



Metasurface integrated optics for fluorescence imaging endoscopy

SUSAN THOMAS,¹ SHANTI BHATTACHARYA,^{1,*}  AND FRANCESCO FERRANTI² 

¹Department of Electrical Engineering, Indian Institute of Technology, Madras, Chennai, India

²Department of Computer Science, Electrical and Space Engineering, Luleå University of Technology, Sweden

*shanti@ee.iitm.ac.in

Abstract: Metasurfaces are shown to offer off-axis optical aberration correction for reflectance imaging in confocal scanning fibre endoscopy. However, in fluorescence imaging, chromatic aberration is a crucial factor that limits image quality. Typically, color correction is achieved by implementing multiple refractive lenses that complicate lens assembly and alignment. In this work, we report the effectiveness of a single metasurface with a gradient refractive index (GRIN) lens for confocal fluorescence imaging, showing significant improvement in image quality. We will show that it is not necessary to correct explicitly for chromatic aberration, as the system is designed such that the excitation and emission wavelengths focus at different planes. This relaxes the need for conventional achromatic correction, as each wavelength is optimised for its respective function. Although two photon endoscopy imaging offers better optical sectioning and imaging performance, higher cost of the source and limited portability of the detection system are some factors that restrict its usage. We implemented a metasurface-integrated aberration-corrected lens system for confocal endoscopy imaging with a compact and portable detection unit and compared the hybrid meta-GRIN lens system to one without a meta-element. The results of reflectance imaging on resolution targets show a 3.5-fold contrast improvement, and fluorescence imaging on biological tissue (mammalian brain) shows a 2-fold increase in the contrast-to-noise ratio at the intermediate to extreme fields (without compromising on-axis performance). The hybrid meta-GRIN lens system achieved a focal spot with a $1/e^2$ beamwidth of 3.1 μm (on-axis) and 3.3 μm (extreme field), over a field of view of 175 $\mu\text{m} \times 40 \mu\text{m}$.

© 2026 Optica Publishing Group under the terms of the [Optica Open Access Publishing Agreement](#)

1. Introduction

Endoscopic imaging devices [1] have been actively researched for improvements in resolution [2], sensitivity, and miniaturization. Visualizing morphological and structural changes at the cellular-level resolution aids early disease diagnosis. Two photon imaging [3] is extensively explored in the regime of endoscopy as it offers better resolution due to the localized excitation and better optical sectioning. However, this technique requires an expensive source, and the detection unit is not simple. Hence, this imaging technique is not suitable for low-resource settings. Confocal laser scanning endoscopy [4] is a suitable and low-cost option for optical imaging at cellular-level resolution and tissue interrogation.

Different imaging modalities are being explored in endoscopy systems. Fibre bundle imaging is the state-of-the-art technique implemented in commercial endoscopy systems. A typical issue with fibre bundle imaging is the honeycomb effect [5] that arises due to the non-imaging space between the cores. An imaging endoscope that uses a GRIN lens in conjunction with a fibre bundle [6] is proposed for fluorescence imaging to visualize lumen morphology in the fallopian tube. Gaussian blur filtering is implemented to reduce the honeycomb effect, and hence, the lateral resolution is limited. In addition, in a fibre bundle, bending can cause core fracture, leading to dead pixels in the displayed image, adding to the cost and maintenance issues. Chip-on-tip

endoscopy [7] is a widely used fibre-free technique that uses a miniature CMOS camera and an LED source at the distal tip of the scope. However, miniature CMOS sensors are too expensive for a single-use purpose, and the image resolution achieved is lower than that defined by the sensor pixels. The fluorescence imaging scope reported in [8] is a multispectral probe that detects multiple fluorophores. However, the imaging of resolution targets shows the effect of geometric distortion (barrel distortion at the corners) and reduced contrast for higher spatial frequencies.

Scanning fibre endoscopy [9] is a low-cost alternative to cellular-level resolution imaging that uses a single fibre for excitation scanning, a set of multi-mode fibres for back-scattered signal collection from the sample, and reconstructs the imaging field based on the reflectance signal. The two different modes, namely widefield reflectance/RGB imaging [10] and NIR fluorescence imaging [11], were explored in use cases such as cholangioscopes [12], angioscopes and bronchoscopes [13] achieving a resolution of the order of 10 - 12 μm with refractive lens triplets or GRIN lenses as microobjective.

Optical aberration is a crucial factor that limits image quality in laser scanning endoscopy systems. Different methods have been adopted for aberration correction in endoscopy imaging. Robert et al. [14] reported a diffractive optical element for phase distortion correction in fibre bundle imaging. However, the validation on the resolution target shows poor contrast due to the lower focus intensity compared to the background intensity. This is because the DOE corrects for only the static phase distortion and does not take into account dynamic phase distortion during scanning. Septier et al. [15] reported nonlinear endoscopy imaging with custom-fabricated aberration-corrected GRIN lenses that use specialized fabrication and tailor the index profile to correct intrinsic aberrations in a GRIN lens. These custom-made GRIN lenses are expensive and do not account for the off-axis aberrations due to scanning. Andrea et al. [16] reported a 3D printed aspherical microlens for PSF correction of GRIN lenses. However, with a PSF corrected lens system, the focal plane is curved and hence cells at the edges of the imaging area lie at different depths.

Recent developments in meta-integrated systems and advanced imaging techniques have been reported in [17–19]. Metalenses have been recently explored in endoscopy applications due to their compactness, especially compared to refractive lenses. J Sun et al. [20], proposed a doublet metalens for off-axis aberration correction, but the meta-atoms are polarization dependent and the performance of the metalens is not demonstrated in an endoscope setup. Song et al. [21] reported on the design of a hybrid refractive-metalens system that can be used with a fibre bundle. However, the lens system includes three metasurfaces, and this has been proposed for confocal imaging at NIR wavelengths. In addition, the fabrication of a metalens integrated hybrid probe and its implementation with a fibre bundle are not evaluated. Xie et al. [22], proposed the implementation of a metalens in a scanning fibre endoscope with a focal length of 400 μm . Although this work demonstrated a large field of view reflectance imaging of a resolution target, the resolution is not close to the cellular level required for imaging of biological samples, and it is not validated for tissue imaging. Moreover, the desired sample end working distance for in vivo confocal or multiphoton imaging is 50-100 μm , beyond which the scattering inside the tissue is too high [23]. Our group [24] has reported the design and validation of a hybrid metasurface GRIN lens system for off-axis aberration correction in a scanning fibre optical system. In a confocal reflectance imaging setup, the excitation spot exhibited a 21% improvement in resolution (extreme field) with the addition of the meta-element.

Another major challenge with the endoscopy system is its conventional photon detection system, especially its bulky footprint due to the requirement for a photomultiplier tube (PMT) and free space dichroic optics. This increases alignment complexity and restricts the portability of this unit. Zhang et al. [25] proposed a single photon endoscope for calcium imaging that uses a GRIN lens as the microobjective, which achieves a FWHM of 10 μm , but the photon detection unit includes dichroic mirrors, emission filters, lenses, and a CMOS sensor for imaging

and is not an easily portable unit. Fei et al. [26], proposed a diffractive lens implemented by tape-based transfer of the lens onto the tip of SMF. Although the lens at the fibre tip achieved a lateral resolution of $2.4\ \mu\text{m}$, validation of only confocal reflectance imaging is reported on a resolution target, as SMF is not a preferred choice for fluorescence collection. Leong et al. [27] reported on a cladding mode detection scheme for backscatter collection for reflectance imaging to analyze the cellular structure of biological plant samples. However, the signal is detected with a photodiode mounted to the fibre cladding, making the distal scanner unit bulky. Chen et al. [28] reported a dual-aperture design for fluorescence excitation and collection. Although fluorescence collection (side view mode) with a double-clad fibre coupler and detection using a spectrometer is demonstrated, fluorescence imaging is not explored in this work.

To the best of our knowledge, confocal fluorescence imaging of biological tissue with metasurface integrated optics for scanning fibre endoscopy in the visible wavelength range (excitation: $640\ \text{nm}$ and emission: $680\ \text{nm}$) has not been reported elsewhere. Our work highlights the use of a double clad fibre and a polarization-independent single metasurface to correct for off-axis aberrations and the effects of chromatic aberrations in a conventional GRIN lens, eliminating the need for custom-fabricated endoscopy GRIN lenses. Unlike conventional chromatic correction [29,30], the goal of the hybrid meta-GRIN lens system is to focus the excitation wavelength at the sample plane and the emission wavelength at the fibre tip plane. In addition to that, the lens combination allows for a much closer working distance ($100\ \mu\text{m}$), desirable for confocal imaging probes. Another major highlight of our work is the clad mode scheme for fluorescence collection and all-fibre optic detection using the coupler and avalanche photodiode (APD), eliminating the need for a PMT and bench-top free-space optics.

2. Optical system for fluorescence detection and imaging

Figure 1 shows the optical system comprising a fibre scanner, lens system for the imaging probe at the distal end, and a detection system at the proximal end. The excitation beam is guided through the core (diameter = $2.3\ \mu\text{m}$) of the double clad fibre towards the sample, and backscattered fluorescence is collected using the lens system into the inner cladding (diameter = $15\ \mu\text{m}$) of the same fibre. The piezoelectric tube is actuated to scan the fibre across the sample.

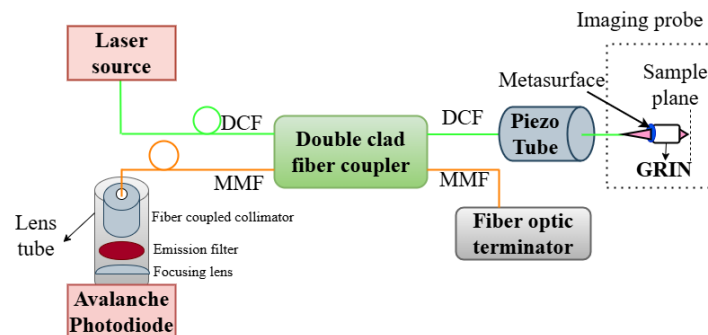


Fig. 1. Benchtop endoscopy optical system for fluorescence imaging

The backscattered signal is guided into the multimode fibre through a double clad fibre coupler (Thorlabs DC530SEFA) and further onto the avalanche photodiode (Thorlabs APD 440A). As the detector surface diameter is $1\ \text{mm}$, a combination of collimator (Thorlabs F240FC-A) and focusing lens (Thorlabs C280TMD-A) is used to focus the light onto the detector. This lens assembly is designed using Zemax and incorporated in a lens tube along with an emission filter (Chroma, ET690) of the center wavelength = $690\ \text{nm}$. The lens assembly takes into account the

beam divergence from the multimode fibre of the coupler and focuses the beam onto the detector surface, improving the fluorescence detection. The lens assembly model in Zemax is discussed in Section 5A of the [Supplement 1](#).

3. Modeling and simulation of phase element integrated lens system

The design of the hybrid meta-GRIN lens system and the optimisation of the phase element that minimizes the monochromatic aberrations (for reflectance imaging) in Zemax sequential ray trace mode are reported [24] in our previous work. Unlike reflectance imaging, which involves single-wavelength excitation and emission, the current work focuses on fluorescence imaging, which involves distinct excitation and emission wavelengths. In the scanning fibre optical system for fluorescence imaging, it is to be noted that the purpose of the phase element is not chromatic focal shift correction. The goal of this lens system is two-fold. Firstly, the optics must focus the excitation wavelength within the smallest possible volume of the sample to maximize excitation. Simultaneously, the smallest possible collection spot must be achieved at the collection fibre.

In our earlier work [31], we studied the optimisation of the phase element at an intermediate wavelength between excitation and emission wavelength. However, we found that the excitation spot quality was compromised. Hence, the phase element was optimised at the excitation wavelength (640 nm). The design methodology is presented in Section 1A of the [Supplement 1](#). Simulation results clearly indicate that the phase element improves the quality of the collection spot. The optimised phase element from sequential ray trace simulations is imported into the non-sequential model (more details in Section 1B of the [Supplement 1](#)) to quantify the fluorescence excitation and emission spot quality.

3.1. Excitation path model

The layout of the hybrid metasurface-GRIN lens system in non-sequential mode is shown in Fig. 2(a). The source object is defined as a source point with a cone angle corresponding to the numerical aperture of the core of the double clad fibre (Thorlabs DCF530, $NA_{core} = 0.11$). The metaoptical element is modeled as a Binary 2 surface with the optimised radial coefficients from the sequential mode analysis of the same optical system.

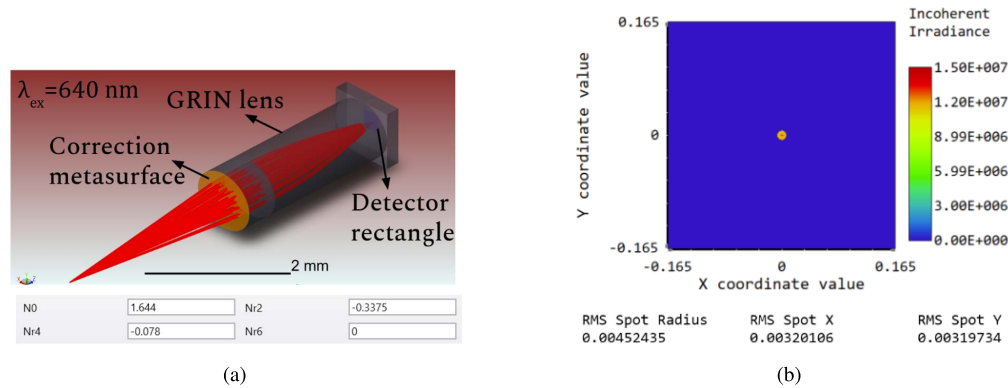


Fig. 2. Ray trace simulation model in non-sequential mode (a) Excitation path model (b) Beam irradiance plot at the sample end (working distance of 100 μm) indicates an RMS spot (X,Y) of 3.2 μm

The GRIN lens is modeled using Eq. (1)

$$n(\lambda_{ref}) = n_o + n_{r2}r^2 + n_{r4}r^4. \quad (1)$$

The GRIN coefficients are known for a reference wavelength (670 nm) from the datasheet of the GRIN lens (Edmund 64524). As dispersion modeling is not directly supported in non-sequential mode, the radial coefficients of the GRIN lens are recomputed at the excitation wavelength (640 nm) using the Sellmeier equation as in Eq. (2).

$$n^2(\lambda) = n^2(\lambda_{ref}) + \sum_{i=1}^3 \frac{K_i(\lambda^2 - \lambda_{ref}^2)}{\lambda^2 - L_i}, \quad (2)$$

where $K_i = \sum_{j=1}^{K_{max}} K_{ij}[n(\lambda_{ref})]^{j-1}$ and $L_i = \sum_{j=1}^{L_{max}} L_{ij}[n(\lambda_{ref})]^{j-1}$.

As we expect isotropic emission from fluorescent beads [32], the scattering at the surface of the sample is defined as Lambertian. The volume physics of the sample is defined using an angle scattering model for the bulk. To model a strongly forward scattering medium, the mean free path and scattering angle are chosen as 0.1 mm and 10° respectively. In the scanning fibre optical setup, the separation between the fibre tip and lens assembly determines the plane of sharpest focus at the sample end. The length from the GRIN lens to that plane is called the sample end working distance. The beam irradiance is evaluated at this distance as well as at the fibre end for illumination and collection paths, respectively. The beam irradiance plots at the sample end working distance (100 μm) are as in Fig. 2(b). The mean free path is varied in the range of 0.005-0.1 mm, representing a dense to sparse distribution of beads, and only 3 % variation in the radial beamwidth was observed at the sample end.

3.2. Collection path model

The sample end irradiance data (detector file) obtained from the excitation path model is loaded at the source end of the collection path model. In addition, the source NA of the model is set at 0.5. The value of NA is chosen on the basis of the maximum angle of acceptance of the GRIN lens. The radial refractive index coefficients of GRIN are recomputed at the collection wavelength of 680 nm and used in this model. The collection path model (sample to fibre) and the beam irradiance plot at the fibre end are shown in Figs. 3(a) and 3(b), respectively. The beam irradiance plot at the fibre end shows a collection spot RMS radius of 7.4 μm , and it was found to be well within the range that can be collected with the diameter of the cladding and the NA of the double clad fibre (diameter = 15 μm , NA = 0.2).

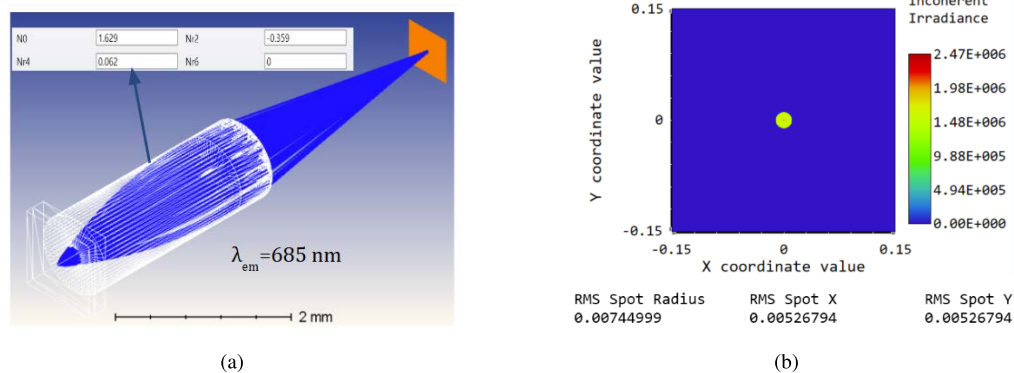


Fig. 3. Ray trace simulations (sample to fibre) (a) Collection path model (b) Beam irradiance plot at the fibre end indicates an RMS spot (X,Y) of 5.2 μm

4. Experimental validations and implementation

4.1. Metasurface for fluorescence collection and imaging

In our previous work, we used polysilicon as the dielectric material for the metasurface. As polysilicon is known to have low transmission efficiency at visible wavelengths, we switched to silicon nitride as a dielectric for the current work. Details of the meta-element and characterization of the fabricated metasurface are presented in Section 2 of the [Supplement 1](#).

4.2. Focus spot characterization in metasurface integrated SFE setup

The spots formed by the GRIN lens alone and the hybrid meta-GRIN lens system are captured using a microscopy setup comprising an objective, tube lens, and camera [24]. To image the focal spot accurately, the working distance of the microscope objective must coincide with the focal spot formed by the GRIN lens/ meta-GRIN lens system. The object working distance (fibre tip to lens) is 3 mm, and the length of the fibre cantilever is 17 mm. Off-axis measurements are taken by applying the maximum DC actuation voltage (250 V) to X electrodes that displace the fibre along the X direction. The extreme field point is estimated from the shift in Peak X position. In this case, the extreme field point is 14 μm from the on-axis. It is evident from the measurement results in [Table 1](#) that after adding the metasurface, there is a percentage decrease of beamwidth by 15.6% (on-axis) and 20.9% (off-axis). Also, the percentage increase in beamwidth from the on-axis to the off-axis is 12.4% in a system where the GRIN lens is the micro-objective, and it is reduced to 5.4% with the addition of the metasurface.

Table 1. Measured focal spot in SFE setup with and without metasurface

Micro-objective	Focal spot $1/e^2$ beamwidth (μm)		Increase in beamwidth relative to on-axis $(\frac{BW_{of}-BW_{on}}{BW_{on}}) \times 100\%$
	On-axis (BW_{on})	Off-axis (BW_{of})	
GRIN lens (BW_g)	3.71	4.17	12.4 %
GRIN lens with metasurface (BW_{mg})	3.13	3.3	5.4 %
Reduction in beamwidth with metasurface $(\frac{BW_g-BW_{mg}}{BW_g}) \times 100\%$	15.6 %	20.9 %	

In the hybrid meta-GRIN lens system, to understand the effect of object working distance on focal spot size and imaging field, the same measurements have been repeated at an object working distance of 2 mm, 3 mm, and the findings are consolidated in [Table 2](#). Varying the object working distance leads to a corresponding shift in the focal spot position. This position, also known as the sample working distance, is determined by translating the microscopy setup as a whole, including the objective, tube lens, and camera. It is clear from the measurements that as the object working distance decreases, the focal spot size increases, and the imaging field increases slightly, albeit with lower resolution.

Table 2. Effect of object working distance on focal spot beamwidth and imaging field

Object working distance (mm)	Focal spot $1/e^2$ beamwidth (μm)		Extreme field position from on-axis (μm)
	on-axis	off-axis	
3	3.13	3.3	14.7
2	4.74	4.79	18.7

4.3. Raster scan generation and image reconstruction

In the focal spot measurements presented in the previous section, the fibre cantilever is actuated with a DC voltage and operated in a non-resonant mode, due to which the extreme field is very small (less than $20\ \mu\text{m}$). To maximize the imaging field for a given fibre cantilever length, the PZT has to be actuated with an AC voltage at the resonance frequency of the fibre cantilever. The fibre cantilever has two distinct resonant modes in the orthogonal directions [33]. To generate a raster scan pattern for scanning across the imaging area, the PZT is to be actuated at these resonances. One pair of the PZT electrodes (corresponding to the vertical scan) is actuated with lower order resonant mode (slow-axis actuation or frame scan). The other pair of electrodes is actuated with a higher-order resonance (fast axis actuation or line scan). For the fibre cantilever length of 17 mm used in our experiment setup, the resonant frequencies were found to be 350 Hz and 1 Hz for line and frame scans, respectively. The ratio of line scan frequency to frame scan frequency is the number of line scans in one frame. With the actuation voltage set at $10\ V_{pp}$ on both axes, the corresponding scan imaging field is found to be $100\ \mu\text{m} \times 50\ \mu\text{m}$. The experiment setup for raster scan generation is provided in Section 3 of the [Supplement 1](#). The Analog Devices module ADALM 2000 is used as a two-channel signal generator to generate the actuation signals on the slow and fast axes. The generated signal is amplified by the TD250 (Micromechatronics) amplifier and then applied to the electrodes of PZT.

The backscattered signal from the sample, collected through the lens system, is directed to the MMF through the coupler. The detection port (MMF) of the coupler is connected to a Si photodiode detector (Thorlabs S120 VC) using a fibre port adaptor (Thorlabs S120 FC). The detected signal is fed to the Tektronix DSO (4 channel, TB2074) along with the actuation signals on the X and Y axes as a reference for data acquisition. Based on our data acquisition for a single line scan with 1785 data points, the X step is calculated as $0.056\ \mu\text{m}$. Similarly, along the vertical direction with 175 line scans and a scan range of $50\ \mu\text{m}$, the Y step is calculated as $0.28\ \mu\text{m}$. The details of the image reconstruction are explained in Section 4 of the [Supplement 1](#). The benchtop scanning fibre probe and lens system is shown in Fig. 4. The metasurface and GRIN lens are placed in a custom 3D printed mount (fabricated at the Central Workshop, IIT Madras).

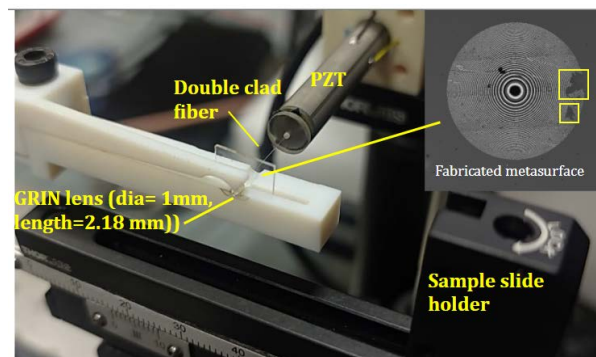


Fig. 4. Benchtop optical system comprising PZT actuated scanning fibre and distal lens system (hybrid meta-GRIN lens). The inset shows the fabricated metasurface (diameter of 1 mm) viewed under microscope. Regions marked in yellow box indicates the missing of meta-atoms.

5. Results

This section discusses the results of reflectance and fluorescence imaging with the metasurface-integrated scanning fibre probe, showing the effectiveness of the meta-element in the correction of aberrations.

5.1. Reflectance imaging of resolution target

The reflectance imaging of a Ronchi Ruling from a standard resolution chart (Thorlabs R2L2S1P1) is performed using the scanning fibre optical system. Reconstructed images corresponding to spatial frequencies of 50, 70, and 150 lp/mm, obtained without and with metasurface in the lens system, are shown in Fig. 5. We analyzed horizontal line profiles along the central and edge regions of the reconstructed images using ImageJ software [34]. We calculated the contrast for a line pair using Eq. (3)

$$C = \frac{I_{max} - I_{min}}{I_{max} + I_{min}}, \quad (3)$$

where I_{max} and I_{min} are the maximum and minimum gray level values in a line pair. The contrast is calculated from line pairs present at the on-axis and off-axis locations (as marked in Fig. 6(a)). The average contrast (calculated from 5 line profiles each) along the central and edge positions with and without metasurface is presented in Table 3. Line profile plots at the edge without and with metasurface are shown in Fig. 6(b) and Fig. 6(c), respectively. The average contrast calculated along the horizontal line profile at the edge shows a 2.75-fold improvement (on-axis) and a 3.5-fold improvement (off-axis) by adding the metasurface.

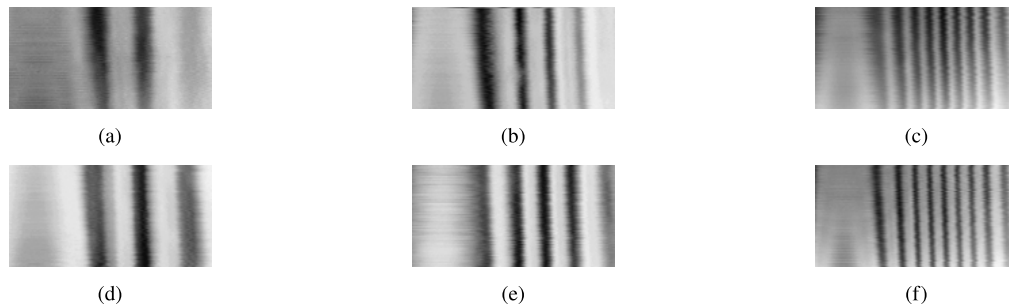


Fig. 5. Reconstructed image (imaging field: $100 \mu\text{m} \times 50 \mu\text{m}$) of line pairs (a), (b), (c) without metasurface (d), (e), (f) with metasurface (same line pairs as in the top row). The line pair widths are (a) & (d) $20 \mu\text{m}$ (b) & (e) $14.28 \mu\text{m}$ (c) & (f) $6.66 \mu\text{m}$.

Table 3. Comparison of contrast calculations for the reconstructed image of 150 lp/mm

Position of the horizontal line profile	Contrast			
	GRIN lens		Meta-GRIN lens	
	on-axis	off-axis	on-axis	off-axis
Central	0.3	0.28	0.53	0.44
Edge	0.16	0.1	0.44	0.35

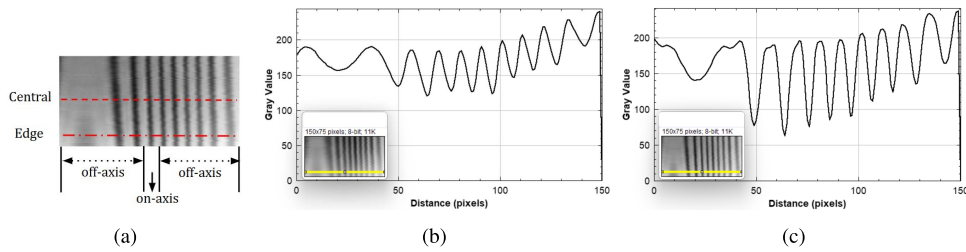


Fig. 6. Horizontal line profile plots and contrast analysis (a) Representation of horizontal line profiles: central and edge indicated by dashed line and dotted dash line respectively, along with on-axis and off-axis locations marked (b) & (c) Line profile plots along edge (b) without meta (c) with meta.

5.2. Fluorescence imaging

5.2.1. Imaging of fluorescent beads

A sample slide mounted with Tetraspeck fluorescent microspheres (Thermo Fisher, T14792) containing different regions marked with microspheres of varying sizes is used for some fluorescence imaging measurements. These microspheres are labeled with four different fluorescent dyes and can therefore be excited at four distinct wavelengths. In our experiment, 640 nm is chosen as the excitation wavelength, with the expected emission centered at 680 nm. The scanning is performed over a region of the slide containing beads with a nominal diameter of 4 μm . A comparison of reconstructed images without and with the metasurface is shown in Fig. 7(a) and 7(b), respectively.

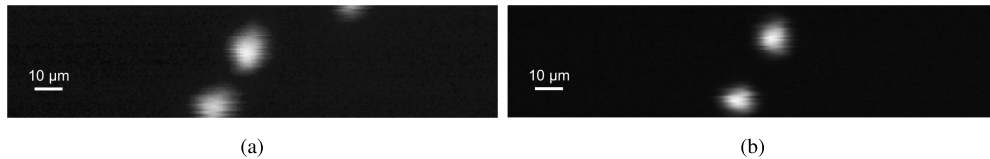


Fig. 7. Fluorescence imaging characterization with fluorescent microspheres and imaging performance comparison of the lens systems for an imaging field of 175 μm x 40 μm (a) with GRIN lens (b) with meta-GRIN lens

The roundness of the beads is evaluated in ImageJ by analyzing the particles in the image after color thresholding. Roundness is defined as the ratio of the minor axis to the major axis of an ellipse fitted to each bead. Based on the reconstructed images of beads at on-axis, intermediate and extreme field points for the cases with and without metasurface (See Fig. S7 in Supplement 1 section 5B), the roundness is evaluated at different field positions and summarized in Table 4. The roundness value is calculated as the average of measurements on 5 different beads at each field point.

Table 4. Quantification of optical aberration and comparison: Roundness of fluorescent beads at different field points.

Case	Roundness		
	on-axis	intermediate	extreme field
GRIN lens	0.68	0.69	0.46
meta-GRIN lens	0.84	0.79	0.91

We applied Lucy-Richardson deconvolution [35] to the reconstructed images (details in Section 5C of the [Supplement 1](#)), and the resulting images were compared with the raw images. Figure 8(a) and Fig. 8(c) show the images before deconvolution without and with the metasurface respectively. As observed in Fig. 8(b), the elongation of the bead at extreme field positions in the GRIN-lens-only system is not corrected by deconvolution. Figure 8(d) shows the reconstructed image acquired with the meta-GRIN lens system after deconvolution, which shows a better roundness of the beads. This result strongly demonstrates the potential of metasurfaces for aberration correction in scanning fibre systems.

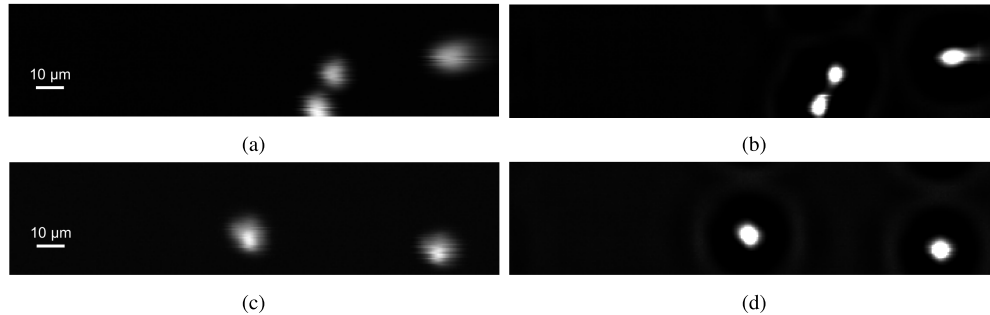


Fig. 8. Fluorescence images before and after deconvolution: Imaging field comprising three beads with GRIN lens (a) raw image (b) after deconvolution. Another imaging field with two beads with meta-GRIN lens (c) raw image (d) after deconvolution

5.2.2. Ex vivo imaging of mouse brain tissue

Additional fluorescence imaging results are based on mouse brain tissue slides prepared (by experts at Sudha Gopalakrishnan Brain Center at IIT Madras, India) using an indirect immunofluorescence protocol. The tissue samples, 20 μm thick, contained neuronal cells labeled with the fluorophore Alexa Fluor 647. The expected emission wavelength is approximately 680 nm. Before imaging the sample slides with our endoscopy optical system, the slides were examined under a confocal fluorescence microscope (Olympus Fluoview 3000). The corresponding images are provided in Section 5D of the [Supplement 1](#). We observed oval-shaped neuronal cells with an average cell size (longer dimension) ranging from 13 to 17 μm in different imaging fields. In our confocal endoscopy optical system, we adjust the laser source power so that the power at the sample end does not exceed 5 mW. We anticipate a transmission loss of around 0.15 as light passes through the meta-element. Ideally, to compare imaging performance with and without the meta-element, both lens systems should deliver the same power to the sample. However, because the light passes through the meta-element twice (excitation path and collection path), it was difficult to match the effective power between the two cases. Therefore, we adjusted the illumination power to be sufficient to excite fluorescence in the tissue sample in the case of the lens system with the metasurface. Later, the meta-element was removed, and the detected signal was acquired without changing the source power. We did not attempt to scale the illumination in the case without the metasurface because the exact power adjustment required to compensate for the metasurface transmission losses was uncertain. Here, in the context of fluorescence imaging, "target" refers to regions that exhibit the fluorescence signal, while "background" refers to regions where no fluorescence is detected. While detecting fluorescence, a constant DC background is observed in the measurements. This baseline value was found to be different in the measurements made with and without the meta-element. To ensure a fair comparison of the optical performance of the two cases, the following procedure was followed. We find the right baseline to be subtracted in each case such that the target-to-background ratio in the central (on-axis) region (marked in yellow

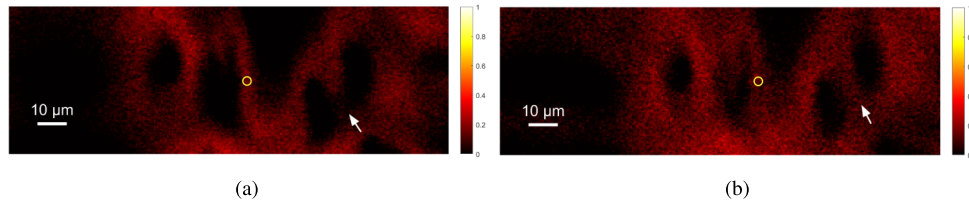


Fig. 9. Reconstructed image of mouse brain tissue slide (Area 1) imaging field: $150 \mu\text{m} \times 50 \mu\text{m}$ (a) with GRIN lens (b) with meta-GRIN lens. The white arrow points to the region where cells are better resolved with meta-GRIN lens. The central region of the imaging field is marked in a yellow circle.

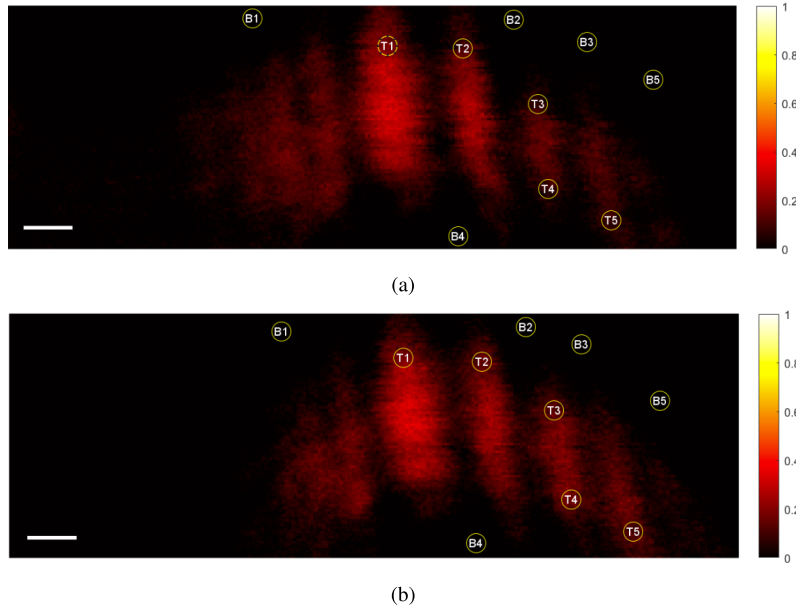


Fig. 10. Reconstructed image of mouse brain tissue slide (imaging field: $150 \mu\text{m} \times 50 \mu\text{m}$) (a) with GRIN lens (b) with meta-GRIN lens system (Scale bar: $10 \mu\text{m}$) The circular ROIs are labeled as T1 to T5 for the target areas, and B1 to B5 for the background areas.

circle in Fig. 9) of the imaging field was the same for both cases. Then we subtract this value from the detected signal in both cases. This scalar subtraction of baseline fluorescence F_o removes only a spatially uniform background. The reconstructed image obtained using our confocal scanning probe is shown in Fig. 9. The white arrow shows where two neuronal cells are resolved better when using the metasurface in the lens system, compared to when not in use. Imaging of a different tissue section revealed well-separated fluorescence peaks as shown in Fig. 10. A circular region of interest (ROI) was selected in both the target area and the background. The mean and variance of these regions were analyzed using ImageJ. The contrast-to-noise ratio (CNR) [36] is calculated using Eq. (4)

$$CNR = \frac{|\mu_T - \mu_B|}{\sqrt{\sigma_T^2 + \sigma_B^2}}, \quad (4)$$

where μ_T , μ_B are the mean intensities, σ_T , σ_B are the standard deviation values in the target and background regions, respectively. Five different regions in the image have been selected to

assess the CNR. Circular ROIs are labeled T1 to T5 for the target areas and B1 to B5 for the background areas. The CNR values calculated for the five regions, CNR_1 to CNR_5 , are given in Table 5. Focusing on the off-axis regions (R2, R3, R4, and R5), there is a two-fold improvement in CNR with the use of meta-element integrated optics. This enhancement indicates that the addition of the meta-element has improved fluorescence collection, resulting in stronger signal strength in the reconstructed image.

Table 5. Contrast to noise ratio for different regions

Case	Contrast to noise ratio				
	CNR_1	CNR_2	CNR_3	CNR_4	CNR_5
GRIN lens	7.5	2.81	2.73	2.61	4.03
Meta-GRIN lens	6.43	6.31	5.46	6.48	5.44

6. Discussions

Various types of neuronal cells are observed in different regions of the mouse brain. Triangular and oval-shaped neurons identified in the cortex region are shown in Fig. 11(a) and 11(b), respectively. In another brain section that contains the hippocampal region, long pyramidal and multipolar neurons were observed, as shown in Figs. 11(c) and 11(d). These reconstructed images are obtained with the metasurface in the distal lens system of our confocal probe. Additional fluorescence imaging results are discussed in Section 5E of the [Supplement 1](#). The different techniques used to enhance the contrast of the reconstructed images are discussed in Section 6 of the [Supplement 1](#). Reflectance imaging is also performed on Nissl-stained brain tissue samples, revealing both neuronal and glial cells; these results are presented in Section 7 of the [Supplement 1](#).

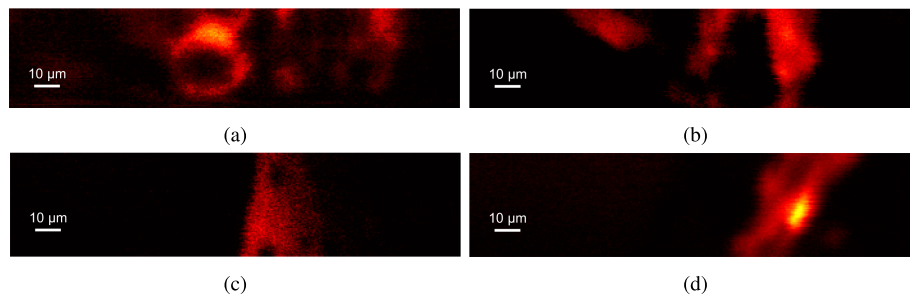


Fig. 11. Reconstructed image (imaging field: $175 \mu\text{m} \times 40 \mu\text{m}$) of various types of neuronal cells obtained from different sections of the brain tissue with aberration corrected lens system for Cortex region (a) round/oval shaped (b) triangular shaped and for Hippocampal region (c) multipolar (d) long pyramidal

There is still room for better imaging performances for the hybrid meta-GRIN approach by further optimising the optical transmission of the metasurface. In addition to that, losses at the meta-GRIN interface are to be minimized. Hence, a careful alignment of the fibre and meta-GRIN lens assembly using custom 3D printed mounts is implemented to optimise the imaging setup. A detailed discussion of fibre-lens alignment is provided in Section 8 of the [Supplement 1](#). The measured efficiency of the metasurface was 85%. (details of the measurements are given in Section 2 of the [Supplement 1](#)). The unit-cell simulations of the meta-atoms predicted a transmittance ranging from 90 to 95%. Furthermore, the unit-cell simulations and the phase lookup table used for metasurface design were computed at a wavelength of 640 nm. Notably, the

metasurface exhibits improved imaging performance despite fluorescence emission occurring at a slightly longer wavelength (680 nm). In addition, there remains scope for further enhancement through improvements in the fabrication process, which could lead to increased metasurface performance. A comparison of our work with recently reported studies in the literature is summarized in Tables 6 and 7.

Table 6. Comparison of our work with recently reported literature (Working distance (in μm) is at the sample end) *data not available **reduced image contrast

System no. [Ref]	Fibre type	Lens system	Resolution (μm)		Working distance
			on-axis	off-axis	
2 [26]	SMF	diffractive lens	2.4	**	235
3 [27]	Dual-core	GRIN lens	3.92	*	1800
4 [37]	Fibre bundle	3D printed lens	8.7	*	500
5 [38]	SMF	Doublet (pair) & half ball lens	1.1	*	*
6 [25]	No fibre	GRIN lens	10	*	*
7 [our work]	DCF (excitation & collection)	meta-GRIN lens	3.13	3.3	100

Table 7. Comparison of the detection system and implementation of our work with recently reported literature (* data not available)

System no. [Ref]	Detection system	Implementation	Reflectance imaging	Fluorescence imaging
1 [22]	MMF to PD	SFE	Resolution grid	No
2 [26]	SMF to PD	not in scope (sample translation)	Ronchi ruling	No
3 [27]	PD mounted on the side of fibre	SFE	Plant cellular morphology	No
4 [37]	fibre bundle relay to proximal camera	fibre bundle	Resolution target, Histology slides	No
5 [38]	Dichroic mirror to PMT	MEMS scan & imaging	*	human colonal mucosa (in vivo)
6 [25]	Dichroic mirror to lens-filter and CMOS sensor	Proximal scan & imaging	*	calcium imaging (in vivo)
7 [our work]	MMF of DCFC to lens-filter assembly to APD	SFE	Ronchi ruling	Beads and Mouse brain tissue (ex vivo)

7. Conclusion

Our study showcases the effectiveness of metasurfaces for off-axis aberration correction while maintaining uniform resolution across the entire imaging field ($175 \mu\text{m} \times 40 \mu\text{m}$), and highlights their successful integration into a scanning fibre optical system with potential applications in confocal fluorescence endoscopy. Though two-photon techniques offer superior resolution, they require expensive laser sources, limiting their practicality. In contrast, we demonstrate a compact confocal endoscopy platform in which the incorporation of a metasurface significantly enhances the fluorescence image contrast across the full field of view. These results were obtained despite

the non-ideal fabrication of the meta-element, resulting in some missing meta-atoms (regions marked in yellow), as seen in the inset of Fig. 4. We believe even better results are possible with a perfect meta-element.

The reported off-axis aberration correction can be extended to two-photon imaging through the design of meta-elements operating at dual wavelengths. Furthermore, the use of a confocal configuration employing a single double-clad fibre for both excitation (core) and signal collection (inner cladding) enables a reduced probe footprint, which is critical for endoscopic applications. The strong fluorescence signal and clear identification of neuronal structures at the periphery of the imaging field underscore the potential of metasurfaces as effective aberration correctors in space-constrained optical systems.

Funding. Department of Higher Education (11/9/2019-U.3(A)).

Acknowledgments. S. Thomas acknowledges the Ministry of Education, India for the research grant through the Prime Ministers Research Fellowship (PMRF). ST and SB thank the Center of Excellence on Healthcare and Assistive Technology for funding. ST and SB also thank Prof. Mohanasankar Sivaprakasam, Dr. Richa Verma, and Ms. Rakshika at the Sudha Gopalakrishnan Brain Center, IIT Madras, for providing the prepared mouse brain tissue sample slide used for imaging. ST and SB gratefully acknowledge the utilization of the BIO-SAIF- Confocal fluorescence microscope in the Common Instrument Facility (CIF) at IIT Madras, in carrying out this research. ST and SB thank Mr. Jerin G. George and the Center for NEMS and Nanophotonics (CNNP) for the fabrication of the meta-element, and the Central Workshop (CWS) for 3D printing.

Disclosures. The authors declare no conflicts of interest.

Data availability. Data underlying the results presented in this paper are not publicly available at this time but may be obtained from the authors upon reasonable request

Supplemental document. See [Supplement 1](#) for supporting content.

References

1. J. M. Jabbour, M. A. Saldua, J. N. Bixler, *et al.*, "Confocal endomicroscopy: Instrumentation and medical applications," *Ann. Biomed. Eng.* **40**(2), 378–397 (2012).
2. E. Abraham, J. Zhou, and Z. Liu, "Speckle structured illumination endoscopy with enhanced resolution at wide field of view and depth of field," *Opto-Electron. Adv.* **6**(7), 220163 (2023).
3. J. C. Jung, A. D. Mehta, E. Aksay, *et al.*, "In vivo mammalian brain imaging using one- and two-photon fluorescence microendoscopy," *J. Neurophysiol.* **92**(5), 3121–3133 (2004).
4. A. L. Polglase, W. J. McLaren, S. A. Skinner, *et al.*, "A fluorescence confocal endomicroscope for in vivo microscopy of the upper- and the lower-gi tract," *Gastrointest. Endosc.* **62**(5), 686–695 (2005).
5. J. Wang, C. Chen, W. You, *et al.*, "Honeycomb effect elimination in differential phase fiber-bundle-based endoscopy," *Opt. Express* **32**(12), 20682–20694 (2024).
6. A. D. Rocha, D. J. Long, W. K. Drake, *et al.*, "First clinical feasibility and safety study of a novel multimodality fallopian tube imaging endoscope," *Lasers Surg. Med.* **57**(2), 163–170 (2025).
7. G. Matz, B. Messerschmidt, W. Göbel, *et al.*, "Chip-on-the-tip compact flexible endoscopic epifluorescence video-microscope for in-vivo imaging in medicine and biomedical research," *Biomed. Opt. Express* **8**(7), 3329–3342 (2017).
8. B. Slomka, S. Duan, T. G. Knapp, *et al.*, "Design, fabrication, and preclinical testing of a miniaturized, multispectral, chip-on-tip, imaging probe for intraluminal fluorescence imaging of the gastrointestinal tract," *Front. Photonics* **3**, 1067651 (2023).
9. E. J. Seibel and Q. Y. J. Smithwick, "Unique features of optical scanning, single fiber endoscopy," *Lasers Surg. Med.* **30**(3), 177–183 (2002).
10. G. Walker, A. P. Wang, P. Z. McVeigh, *et al.*, "The scanning fiber endoscope: A novel surgical and high-resolution imaging device for intracranial neurosurgery," *Oper. Neurosurg.* **23**(4), 326–333 (2022).
11. L. E. Savastano and E. J. Seibel, "Scanning fiber angiography," *Neurosurgery* **64**(CN_suppl_1), 188–198 (2017).
12. T.-S. Chang, Y. Zhou, R. Zhang, *et al.*, "Flexible fiber cholangioscope for detection of near-infrared fluorescence," *VideoGIE* **8**(3), 110–112 (2023).
13. C. M. Lee, C. J. Engelbrecht, T. D. Soper, *et al.*, "Scanning fiber endoscopy with highly flexible, 1 mm catheterscopes for wide-field, full-color imaging," *J. Biophotonics* **3**(5-6), 385–407 (2010).
14. R. Kuschmierz, E. Scharf, D. F. Ortégón-González, *et al.*, "Ultra-thin 3d lensless fiber endoscopy using diffractive optical elements and deep neural networks," *Light: Advanced Manufacturing* **2**(4), 415–424 (2021).
15. D. Septier, G. Brévalle-Wasilewski, E. Lefebvre, *et al.*, "A hollow-core fiber based stand-alone multimodal (2-photon, 3-photon, shg, thg) nonlinear flexible imaging endoscope system," *IEEE J. Sel. Top. Quantum Electron.* **30**(6: Advances and Applications), 1–12 (2024).

16. A. Antonini, A. Sattin, M. Moroni, *et al.*, “Extended field-of-view ultrathin microendoscopes for high-resolution two-photon imaging with minimal invasiveness,” *eLife* **9**, e58882 (2020).
17. Y. Zhou, Z. Chen, J. Cheng, *et al.*, “High-resolution 3d imaging with tunable point cloud projection based on meta-device,” *Laser Photonics Rev.* **20**(2), e01327 (2026).
18. X. Liu, J. Zhang, B. Leng, *et al.*, “Edge enhanced depth perception with binocular meta-lens,” *Opto-Electron. Sci.* **3**(9), 230033 (2024).
19. Z. Zhao, X. Liu, Y. Ji, *et al.*, “Meta-lens digital image correlation,” *Opto-Electron. Adv.* **8**(9), 250014 (2025).
20. J. Sun, W. Shen, J. Wang, *et al.*, “High-resolution and wide-field microscopic imaging with a monolithic meta-doublet under annular illumination,” *Adv. Photonics* **7**(04), 046006 (2025).
21. Y. Song, S. Mao, Y. Tang, *et al.*, “Metalens-based hybrid probe near-infrared endoscope objective,” *Opt. Express* **33**(3), 5757–5768 (2025).
22. N. Xie, Z. Zhou, J. E. Fröch, *et al.*, “Inverse-designed large field-of-view polychromatic metalens for tri-color scanning fiber endoscopy,” *Commun. Eng.* **4**(1), 53 (2025).
23. R. Richards-Kortum, C. Lorenzoni, V. S. Bagnato, *et al.*, “Optical imaging for screening and early cancer diagnosis in low-resource settings,” *Nat. Rev. Bioeng.* **2**(1), 25–43 (2023).
24. S. Thomas, J. G. George, F. Ferranti, *et al.*, “Metaoptics for aberration correction in microendoscopy,” *Opt. Express* **32**(6), 9686–9698 (2024).
25. J. Zhang, R. N. Hughes, N. Kim, *et al.*, “A one-photon endoscope for simultaneous patterned optogenetic stimulation and calcium imaging in freely behaving mice,” *Nat. Biomed. Eng.* **7**(4), 499–510 (2022).
26. F. He, R. Fuentes-Domínguez, R. Cousins, *et al.*, “Scalable fabrication of single- and multi-layer planar lenses on fiber imaging probes,” *APL Photonics* **10**(5), 056114 (2025).
27. Y. S. Leong, M. H. H. Mokhtar, M. S. D. Zan, *et al.*, “Enhancement of in-vitro cellular structure morphology imaging using multiwavelength confocal endoscopic scanner,” *Alex. Eng. J.* **97**, 14–24 (2024).
28. R. Chen, F. Rothermel, R. Fitridge, *et al.*, “Low background fluorescence 3d-printed micro-lens for imaging of vulnerable atherosclerotic plaques,” *APL Photonics* **10**(4), 040805 (2025).
29. W. T. Chen, A. Y. Zhu, V. Sanjeev, *et al.*, “A broadband achromatic metalens for focusing and imaging in the visible,” *Nat. Nanotechnol.* **13**(3), 220–226 (2018).
30. R. J. Lin, V.-C. Su, S. Wang, *et al.*, “Achromatic metalens array for full-colour light-field imaging,” *Nat. Nanotechnol.* **14**(3), 227–231 (2019).
31. S. Thomas, F. Ferranti, and S. Bhattacharya, “Meta-element-enhanced confocal scanning fiber fluorescence endoscopy optical system,” in *Endoscopic Microscopy XXI*, vol. 13866 (SPIE, 2026).
32. L. A. Alemán-Castañeda, S. Y. Feng, R. Gutiérrez-Cuevas, *et al.*, “Using fluorescent beads to emulate single fluorophores,” *J. Opt. Soc. Am. A* **39**(12), C167–C178 (2022).
33. D. Do, H. Yoo, and D.-G. Gweon, “Fiber-optic raster scanning two-photon endomicroscope using a tubular piezoelectric actuator,” *J. Biomed. Opt.* **19**(6), 066010 (2014).
34. C. A. Schneider, W. S. Rasband, and K. W. Eliceiri, “Nih image to imagej: 25 years of image analysis,” *Nat. Methods* **9**(7), 671–675 (2012).
35. N. Dey, L. Blanc-Féraud, C. Zimmer, *et al.*, “Richardson-lucy algorithm with total variation regularization for 3d confocal microscope deconvolution,” *Microsc. Res. Tech.* **69**(4), 260–266 (2006).
36. K. M. Kempfski, M. T. Graham, M. R. Gubbi, *et al.*, “Application of the generalized contrast-to-noise ratio to assess photoacoustic image quality,” *Biomed. Opt. Express* **11**(7), 3684–3698 (2020).
37. D. Galvez, Z. Hong, A. D. Rocha, *et al.*, “Characterizing close-focus lenses for microendoscopy,” *J. Optical Microsystems* **3**(01), 011003 (2023).
38. M. Lee, G. Li, H. Li, *et al.*, “Confocal laser endomicroscope with distal mems scanner for real-time histopathology,” *Sci. Rep.* **12**(1), 20155 (2022).